
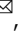






Atomic-scale imaging of $\text{CH}_3\text{NH}_3\text{PbI}_3$ structure and its decomposition pathway

Shulin Chen^{1,2,12}, Changwei Wu^{3,12}, Bo Han¹, Zhetong Liu¹, Zhou Mi⁴, Weizhong Hao⁴, Jinjin Zhao⁴ [✉],
Xiao Wang^{3,5} [✉], Qing Zhang⁶ [✉], Kaihui Liu^{7,8} [✉], Junlei Qi², Jian Cao², Jicai Feng², Dapeng Yu⁹,
Jiangyu Li^{3,5,10} [✉] & Peng Gao^{1,8,11} [✉]

Understanding the atomic structure and structural instability of organic-inorganic hybrid perovskites is the key to appreciate their remarkable photoelectric properties and understand failure mechanism. Here, using low-dose imaging technique by direct-detection electron-counting camera in a transmission electron microscope, we investigate the atomic structure and decomposition pathway of $\text{CH}_3\text{NH}_3\text{PbI}_3$ (MAPbI₃) at the atomic scale. We successfully image the atomic structure of perovskite in real space under ultra-low electron dose condition, and observe a two-step decomposition process, i.e., initial loss of MA⁺ followed by the collapse of perovskite structure into 6H-PbI₂ with their critical threshold doses also determined. Interestingly, an intermediate phase (MA_{0.5}PbI₃) with locally ordered vacancies can robustly exist before perovskite collapses, enlightening strategies for prevention and recovery of perovskite structure during the degradation. Associated with the structure evolution, the bandgap gradually increases from ~1.6 eV to ~2.1 eV. In addition, it is found that C-N bonds can be readily destroyed under irradiation, releasing NH₃ and HI and leaving hydrocarbons. These findings enhance our understanding of the photoelectric properties and failure mechanism of MAPbI₃, providing potential strategies into material optimization.

¹Electron Microscopy Laboratory, International Center for Quantum Materials, School of Physics, Peking University, Beijing, China. ²State Key Laboratory of Advanced Welding and Joining, Harbin Institute of Technology, Harbin, China. ³Shenzhen Key Laboratory of Nanobiomechanics, Shenzhen Institute of Advanced Technology, Chinese Academy of Sciences, Shenzhen, China. ⁴School of Materials Science and Engineering, School of Mechanical Engineering, Shijiazhuang Tiedao University, Shijiazhuang, China. ⁵Department of Materials Science and Engineering, Southern University of Science and Technology, Shenzhen, China. ⁶Department of Materials Science and Engineering, College of Engineering, Peking University, Beijing, China. ⁷State Key Laboratory for Mesoscopic Physics, School of Physics, Peking University, Beijing, China. ⁸Collaborative Innovation Center of Quantum Matter, Beijing, China. ⁹Department of Physics, South University of Science and Technology, Shenzhen, China. ¹⁰Guangdong Provisional Key Laboratory of Functional Oxide Materials and Devices, Southern University of Science and Technology, Shenzhen, China. ¹¹Interdisciplinary Institute of Light-Element Quantum Materials and Research Center for Light-Element Advanced Materials, Peking University, Beijing, China. ¹²These authors contributed equally: Shulin Chen, Changwei Wu. ✉email: jinjinzhao2012@163.com; xiao.wang@siat.ac.cn; lijy@sustech.edu.cn; p-gao@pku.edu.cn

Organic-inorganic hybrid perovskites (OIHPs) have attracted great research interests as promising materials for the next generation photovoltaic energy harvesting^{1,2}, electro-optic detection^{3,4} and all-optical conversion^{5,6}. Their remarkable properties are underpinned by atomic structures of hybrid perovskites⁷, ABX_3 , with organic species such as $CH_3NH_3^+$ (MA^+) and $CH(NH_2)_2^+$ (FA^+) occupying A-site and inorganic Pb^{2+} in B-site surrounded by X-octahedron formed by halogen elements like I^- and Br^- . In particular, the corner-sharing $[PbI_6]^{4-}$ octahedron is believed to be beneficial for carrier diffusion^{8,9}, while its distortion under chemical strain¹⁰ makes the band gap tunable, ideal for photovoltaic conversion. Moreover, the organic cations as well as the hydrogen bonding may lead to spontaneous polarization and ferroelectricity¹¹, which promotes the separation of photoexcited electron-hole pairs, and thus reduces the recombination and improves the carrier lifetime¹². These characteristics are responsible for the promising optoelectronic properties including high carrier mobility, long charge diffusion length and superior power conversion efficiency¹³. Nevertheless, the exact atomic structure of OIHPs is still unsettled, with two possible space groups, polar $I4cm$ and nonpolar $I4/mcm$ still hotly debated depending on the orientations of polar ions such as MA^+ ¹⁴. While many perovskite oxides are polar with strong ferroelectricity, the polarity of OIHPs has yet to be firmly established¹⁵.

The lack of detailed understanding on atomic structure of OIHPs is largely due to the incapability to image OIHPs at the atomic scale^{16,17}. It is well known that OIHPs are quite unstable and prone to decomposition under electron beam irradiation^{18–21}. While much progress has been made in transmission electron microscopy (TEM) characterizations of OIHPs, direct visualization of atomic structure remains to be elusive. Initial TEM studies at low doses are mainly observing the morphology evolutions¹⁸ and structure transitions by reciprocal-space electron diffraction (ED) techniques^{19,20}, and many of the earlier studies mislabeled the decomposition product PbI_2 as $MAPbI_3$ ^{22–24}. With the help of direct-detection electron-counting (DDEC) camera, high-resolution TEM (HRTEM) image of $CH_3NH_3PbBr_3$ has been successfully obtained, which is much more stable than $MAPbI_3$, though the observed off-centered MA^+ with different orientations has not been well substantiated¹⁶. Recently, low-dose scanning transmission electron microscopy (STEM) technique provides atomic-scale insights into crystalline defects of $CH(NH_2)_2PbI_3$

($FAPbI_3$), though the obtained atomic structures have already been damaged due to the large doses involved ($53–221 e \text{ \AA}^{-2}$)²⁵. Cryo-HRTEM has been used to image $MAPbI_3$ at $100 e \text{ \AA}^{-2}$, yet the corresponding fast Fourier transform (FFT) pattern lacks (002) reflection, indicating substantial beam damage²⁶. Furthermore, Li et al. found that superstructure reflections, a sign of structural transition due to beam damage, have already appeared at a dose as low as $7.6 e \text{ \AA}^{-2}$ (Ref. 27), and under Cryo-TEM, rapid amorphization has also been observed^{18,28}. Indeed, the damage-free pristine structure of $MAPbI_3$ has not been imaged at the atomic scale, and the corresponding real-space degradation pathway is yet to be established, thus motivating this study.

It is well known that STEM imaging introduces comparably larger dose and damage than low-dose HRTEM, while the contrast of HRTEM is sensitive to imaging condition, making it difficult to identify the specific atomic columns of $MAPbI_3$ ²⁹. To overcome these difficulties, we adopted DDEC camera combined with an imaging technique using a negative value of the spherical-aberration coefficient³⁰, and we have successfully captured the atomic structure of $MAPbI_3$ in real space at a dose as low as $0.7 e \text{ \AA}^{-2}$, ensuring minimum beam damage if any. We further observed a two-step degradation pathway at the atomic scale, initiated with the loss of MA^+ to form a superstructure $MA_{0.5}PbI_3$ with ordered MA^+ vacancies (V_{MA}^-), followed by the diffusion of I^- and Pb^{2+} to form the decomposed $6H-PbI_2$, with the corresponding critical doses also identified. During the process, C–N bonds can be destroyed under irradiation, releasing NH_3 and HI and leaving hydrocarbons. The continuous structure transformations result in gradually increased bandgap, which is confirmed by scanning electron microscope cathodoluminescence (SEM-CL) experiments and validated by density functional theory (DFT) calculations. The direct visualization of the structure and degradation process at the atomic scale provides valuable sights into understanding the properties and stability of OIHPs. Furthermore, the emergence of superstructure before the collapse of perovskite framework also points toward a strategy for stabilizing the materials during the degradation.

Results

Identification of damage-free threshold dose. $MAPbI_3$ nanocrystals with 10–20 nm size and good crystalline (Supplementary

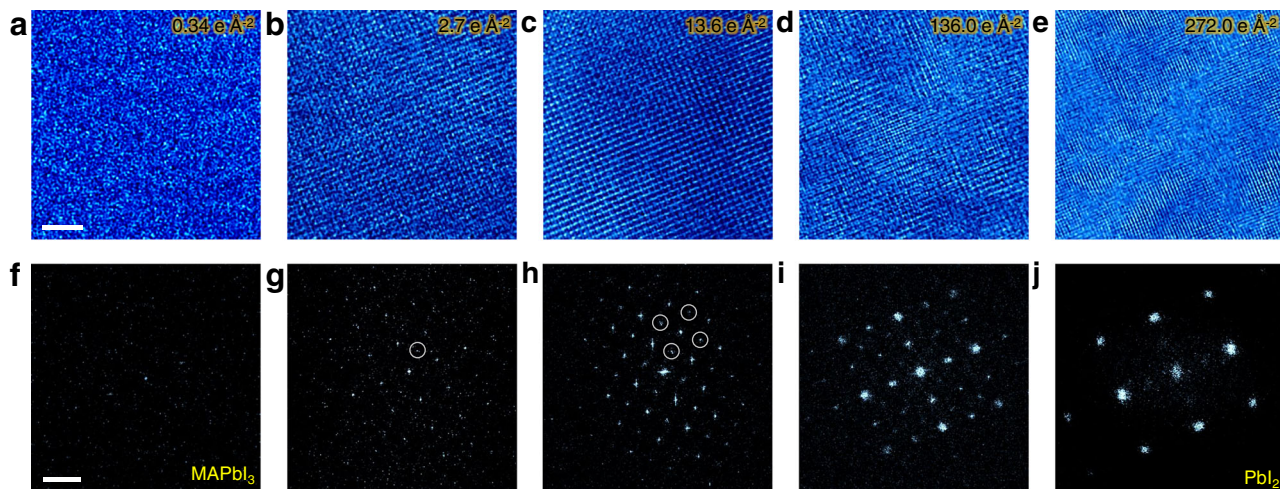


Fig. 1 Tracking structure evolution during the decomposition of $MAPbI_3$. **a–e** Time-series HRTEM images during the degradation of $MAPbI_3$ under electron beam irradiation. The corresponding doses are marked on each panel. Scale bar, 4 nm. **f–j** The corresponding FFT patterns from $MAPbI_3$ to $6H-PbI_2$. Circles indicate the superstructure diffraction reflections. Scale bar 2 nm^{-1} .

Fig. 1) are chosen for low-dose imaging. Using DDEC camera, HRTEM images of MAPbI₃ can be acquired at low doses as shown in Fig. 1. It is noted that sufficient dose (Supplementary Fig. 2) is needed to obtain images with good quality and superstructure diffraction reflections appear due to the generation of intermediate phases when the dose is larger than 2.7 e Å⁻² (Fig. 1b, g). Judging from the corresponding FFT patterns, the [001] MAPbI₃ with intermediate phases gradually transforms at 13.6 e Å⁻², and finally decomposes into [441] or [481] 6H-PbI₂ (Supplementary Fig. 3) at 272.0 e Å⁻². Such a 6H-PbI₂ product has also been observed during the degradation of polycrystal MAPbI₃²¹. Thus the threshold dose for MAPbI₃ without forming superstructures is determined to be 2.7 e Å⁻² while 272.0 e Å⁻² for the complete decomposition into PbI₂. These determined doses can guide the future TEM characterizations of MAPbI₃, especially for in situ ones such as under heat, electric field etc, for which the effect of electron beam irradiation is generally more significant due to the larger dose.

Atomic-imaging of MAPbI₃ structure and the intermediate phase. We then investigate the atomic structure via an imaging technique using a negative value of the spherical-aberration coefficient (Cs), which has enabled the successful observation of both light and heavy elements in oxide perovskite³⁰. Figure 2a is the HRTEM image acquired at a negative Cs with an overfocus, wherein the brightest 'I' column, second brightest 'II' column and the darkest 'III' column can be distinguished. By comparing the atomic structure features of MAPbI₃ (Fig. 2b) and HRTEM simulations (Supplementary Fig. 4), 'I', 'II' and 'III' columns are identified to be Pb²⁺-I⁻, I⁻ and MA⁺, respectively. With increased dose, the intensity of MA⁺ is decreased at 10.5 e Å⁻² as shown in Fig. 2c. The quantitative intensity analysis (Fig. 2d) further verifies that the intensity of MA⁺ progressively decreases within the initial 10.5 e Å⁻², and then remains stable until 28.0 e Å⁻² before subsequent gradual increase (Supplementary Fig. 5). The decreased intensity is caused by the formation of V_{MA}⁻³¹ while the unchanged intensity is likely resulted from a relatively

stable intermediate phase with the preserved perovskite framework. The subsequently increased intensity is resulted from the diffusion of I⁻ and Pb²⁺, as discussed in the following. Figure 2e and Supplementary Fig. 6 further show V_{MA}⁻ appears at every other 'III' column, as illustrated in Fig. 2f. Such a cation-vacancy-ordered structure with superstructure reflections (Supplementary Fig. 7) corresponds to MA_{0.5}PbI₃, whose stability is verified by molecular dynamic simulation (Supplementary Fig. 8). Accordingly, it is concluded that the loss of MA⁺ starts even at 1.0 e Å⁻² and reaches a balanced state between ~10.5 and 28.0 e Å⁻² to form ordered V_{MA}⁻, wherein the perovskite structure framework is preserved.

Evolution of the electronic structure and chemical bonding.

The effect of ordered V_{MA}⁻ on its electronic structure is further investigated. Figure 3a, b show the calculated band structure of MAPbI₃ and MA_{0.5}PbI₃. The band gap of MAPbI₃ is 1.56 eV while it is 1.69 eV for MA_{0.5}PbI₃. The increased band gap is caused by the enhanced hybridization between I⁻-5p and Pb²⁺-6p atomic orbitals and the conduct band minimum shifting about 0.1 eV to the high energy level, as explained in Supplementary Fig. 9. To confirm this analysis, we also carried out SEM CL experiments. Supplementary Fig. 10 shows the initial CL emission with a single excitonic peak at the photon energy of ~1.58 eV. Time-series CL emissions in Fig. 3c show that the observed peaks gradually become broader and shift to higher energy (2.05 eV) with the excitonic peak intensity decreasing. Such blue-shift is associated with the electron-beam-induced phase transformations³², i.e., forming the intermediate phases and decomposing into 6H-PbI₂, considering that the calculated bandgaps of MAPbI₃, MA_{0.5}PbI₃ and 6H-PbI₂ are 1.56, 1.69, and 2.15 eV (Supplementary Fig. 11), respectively, in good agreement with the experimental observation.

In addition to electronic structure evolutions, it is worth investigating how the chemical bonding within organic components evolves (Fig. 3d, e) during the degradation. Vibrational electron energy loss spectroscopy operated at 'aloo' mode³³

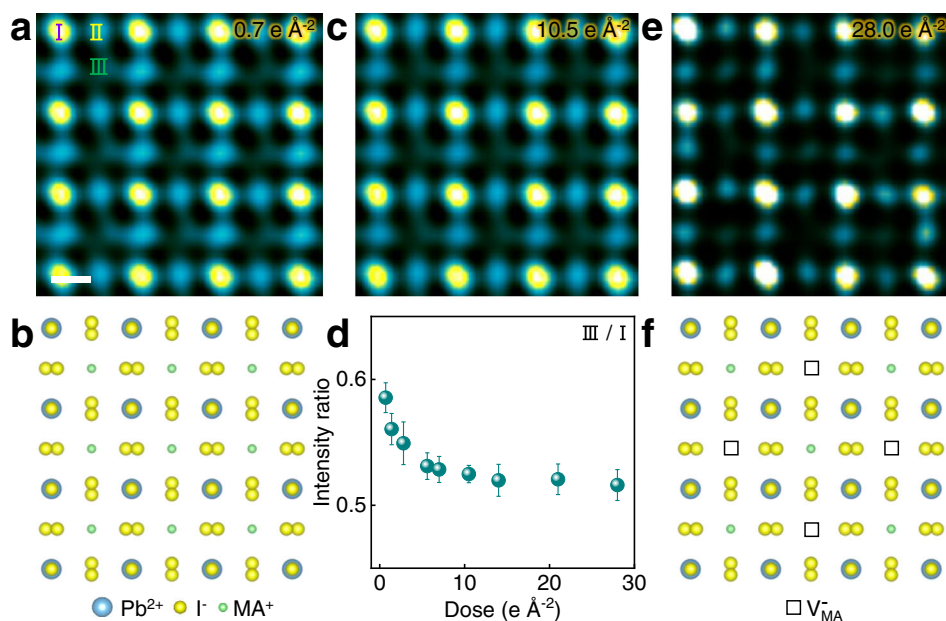


Fig. 2 Atomic-imaging of the loss of MA⁺ and intermediate phase. **a** HRTEM image acquired at 0.7 e Å⁻². 'I', 'II' and 'III' columns correspond to Pb²⁺-I⁻, I⁻, and MA⁺ columns respectively. Scale bar, 3 Å. **b** Structural model of tetragonal MAPbI₃. **c** HRTEM image acquired at 10.5 e Å⁻². **d** Intensity ratio of 'III' to 'I' column with increased doses. Nine data points of 'III' and 'I' type columns are used to obtain nine intensity ratios at each dose. The error bars represent standard deviations. **e** HRTEM image acquired at 28.0 e Å⁻². **f** Structural model of MA_{0.5}PbI₃. The squares indicate V_{MA}⁻.

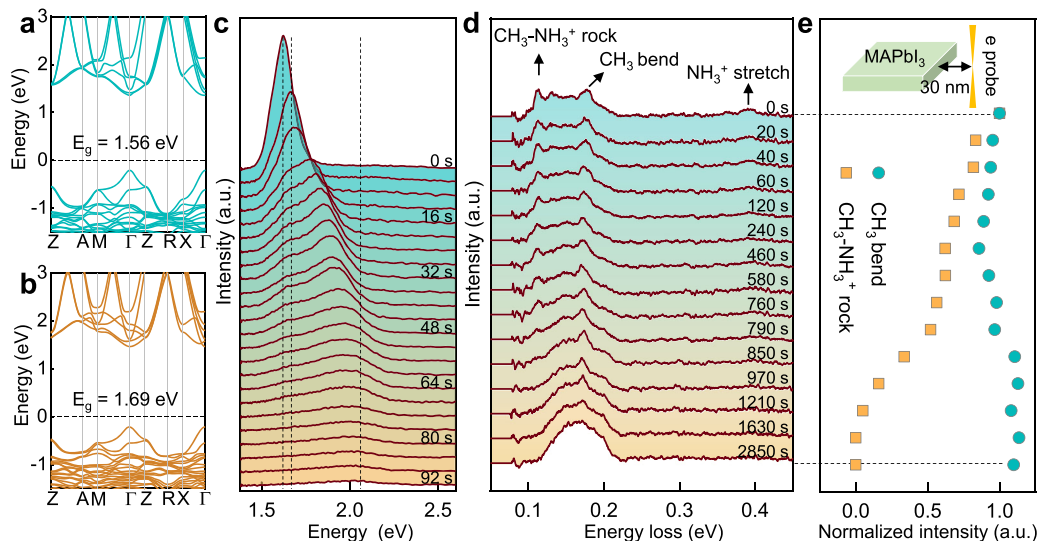


Fig. 3 Electronic structure and chemical bonding evolutions during the degradation. **a, b** Electronic structures of MAPbI₃ and MA_{0.5}PbI₃. The Fermi level is set to zero. **c** Time-series CL spectra showing the bandgap gradually increases from 1.6 eV to 2.05 eV. The dashed lines show the calculated bandgaps at 1.56, 1.69 and 2.15 eV for MAPbI₃, MA_{0.5}PbI₃ and 6H-PbI₂, respectively. **d** Time-series vibrational spectra under ‘aloof’ mode with the electron probe ~30 nm away from MAPbI₃. Black arrows indicate the peaks related with CH₃-NH₃⁺ rock, CH₃ bend and NH₃⁺ stretch. The background was subtracted by the power-law function. **e** Evolutions of normalized intensities of CH₃ bending (cyan circles) and CH₃-NH₃⁺ rock (orange squares) during the degradation. Inset is the schematic diagram of ‘aloof’ mode showing the electron probe is ~30 nm away from MAPbI₃ for the vibrational spectroscopy measurements.

(inset of Fig. 3e), which enables the control of damage by changing the distance between electron beam and sample³³, is used to obtain the characteristic vibrational modes of MAPbI₃ (Fig. 3d). We can observe the vibrational signals of CH₃-NH₃⁺ rock at 113 meV, CH₃ bend at 177 meV, and NH₃⁺ stretch at 391 meV³⁴. Time-series vibrational spectra show that the peaks of CH₃-NH₃⁺ rock and NH₃⁺ stretch gradually disappear with increased time, suggesting the breakage of chemical bonds and/or escape of the certain gas. The extracted intensities of C–N and C–H bonds are shown in Fig. 3e and the processing details are shown in Supplementary Fig. 12. It is observed that the intensity of C–H bonds does not decrease during the degradation, suggesting the negligible release of carbonaceous gas. Such C–H bend signals can come from (–CH₂–CH₂–)^{35–37} or CH₃I, while previous energy-dispersive spectroscopy¹⁹ and X-ray photoelectron spectroscopy³⁸ results show that the atomic ratio of I to Pb for the beam-induced decomposition product is ~2, suggesting it to be PbI₂ instead of CH₃I. Thus, the C–H bend signal in the final byproduct likely comes from (–CH₂–CH₂–)^{35–37}. In addition, the peak of CH₃-NH₃⁺ rock gradually disappears, suggesting its breakage, which leads to the formation and escape of volatile NH₃, further explaining the gradually decreased intensity of the N–H bond (Fig. 3d) and the drop of N content to 0 (Ref. 38). Such degradation process has also been proposed in the previous study based on the exposure to moisture³⁹, indicating similarities in degradation mechanism between the electron beam irradiation and other stimuli.

Atomic-scale observation of I[–] and Pb²⁺ diffusion. Based on above study, we further investigate the atomic-scale decomposition pathway of MAPbI₃. Figure 4a is the structure of perovskite with V_{MA}[–], as illustrated in Fig. 4e. With increased doses, it is observed that the intensities of these three columns gradually change (Fig. 4b–d). A quantitative analysis of the intensity changes (Supplementary Fig. 13) shows that the intensities of ‘I’ columns initially increase and then gradually decrease while the intensities of ‘II’ columns continuously increase and the intensities of ‘III’ columns initially decrease and then gradually

increase. Finally, intensities of all three type columns converge, indicating the formation of PbI₂. The initial intensity decrease of MA⁺ column results from the formation of V_{MA}[–], while the following increased intensity of MA⁺ column and decreased intensity of Pb²⁺-I[–] column are believed to be caused by two kinds of I[–] and Pb²⁺ diffusion as illustrated in Fig. 4f. One is the diffusion of I[–] and Pb²⁺ into V_{MA}[–] (Supplementary Fig. 14) while the other is caused by the [PbI₆]^{4–} octahedron slipping from corner sharing to edge sharing. Finally, the structure gradually evolves to PbI₂. Figure 4e–g illustrate the atomic-scale structural evolution and the related ion migration during the decomposition from MAPbI₃, MA_{0.5}PbI₃, to the final PbI₂, mainly involving two processes, forming V_{MA}[–] and the collapse of perovskite structure via the diffusion of Pb²⁺ and I[–]. While previous literature²¹ proposed a two-step transformation of polycrystalline MAPbI₃: Pb-related defects form at grain boundary and then phase transforms into PbI₂, here we have observed an intermediate phase with locally ordered MA⁺ vacancies and revealed the atomic-scale decomposition pathway from MAPbI₃ into PbI₂, which enhances our understanding on the OIHPs’ degradation.

Discussion

The extreme beam sensitivity of OIHPs hinders atomic-resolution imaging and thus the detailed investigations on their structure-property relationships. By DDEC camera, we have determined that the threshold dose for superstructure formation is about 2.7 e Å^{–2}, and perovskite collapses into PbI₂ within 272.0 e Å^{–2}, both of which are smaller than those measured by ED¹⁹. This is mainly because ED pattern is obtained from a comparably larger region and represents the average information. These threshold conditions can guide future TEM characterizations and encourage more atomic-scale investigations about OIHPs.

Atomic-scale imaging of MAPbI₃ and its degradation pathway allows us to better understand properties of OIHPs. For example, the observed off-center displacements (up to ~30 pm) between different atom columns likely indicate the polar nature of this material⁴⁰, although further studies are needed to fully clarify this

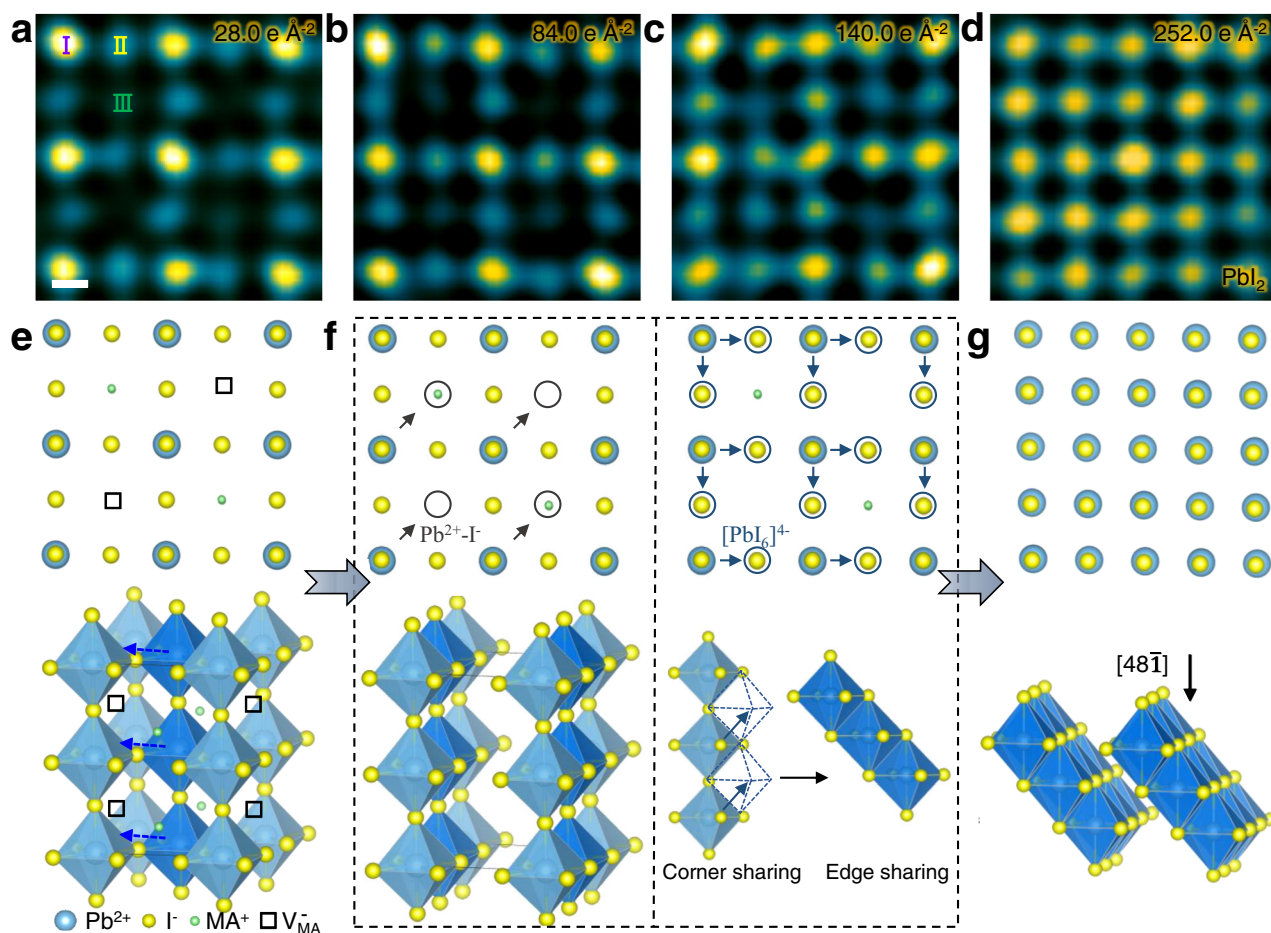


Fig. 4 Atomic-scale imaging of the decomposition pathway. **a–d** HRTEM images with increased doses during the degradation into PbI_2 . The corresponding doses are marked on each panel. Scale bar, 2 Å. **e** Atomic structure of $\text{MA}_{0.5}\text{PbI}_3$. Black squares indicate V_{MA}^- . **f** Atomic structures to illustrate two kinds of I^- and Pb^{2+} diffusion. Left panel shows I^- and Pb^{2+} diffusing to V_{MA}^- while the right panel illustrates the $[\text{PbI}_6]^{4-}$ octahedron slipping from corner sharing to edge sharing. **g** Atomic structure of PbI_2 .

point, including determining MA^+ configuration¹⁵ and quantifying the effects from possible mistilt and residual aberrations⁴¹. Furthermore, from the energetic point of view, the electron beam can transfer energy to the materials, enable ions to overcome the diffusion barrier and thus induce structure transformations, which is similar to heat- or light-induced phase transformations and degradation. For example, the decomposition of MAPbI_3 into PbI_2 with the release of NH_3 and HI ³⁸ has also been observed under light illumination⁴² and moisture atmosphere³⁹. In addition, the increase of bandgap during the degradation has also been observed under illumination^{43,44}. Therefore, our investigation of electron beam-induced decomposition pathway can also help understand how the devices fail in practical working conditions. Besides, the superstructure phase with additional reflections has been previously reported to be likely related with octahedra tilts¹⁸ or ordered iodine vacancies¹⁹ based on reciprocal-space ED analysis, our atomic-resolution imaging, however, has suggested that cation-ordered vacancies are more likely. Such an intermediate phase ($\text{MA}_{0.5}\text{PbI}_3$) with locally ordered vacancies can stably exist before perovskite collapses, suggesting the degraded structure with partial formation of V_{MA}^- may be recovered. This likely sheds light into reversible photo-induced structural changes without forming PbI_2 ⁴⁵. Such self-healing behavior under illumination has also been observed in MAPbI_3 -based solar cells⁴⁶. In addition, the loss of MA^+ causes

the increase of bandgap, which provides a potentially new strategy to tune the bandgap in constructing tandem solar cells⁴⁷. Also, the increased bandgap facilitates multiwave electroluminescence emission, adjusting various color luminescence under increasing bias voltage^{4,48}.

Ion migration in OIHP-based electronic device is regarded as one of the most important processes, which contributes to the phase segregation, hysteresis in J-V curves and device degradation⁴⁹. Previous studies about ion migration are either based on calculations or macro-measurements⁴⁹ like time of flight secondary ion mass spectroscopy⁵⁰, conductive atomic force microscopy⁵¹, and energy-dispersive X-ray mappings^{52,53}, all without achieving the atomic-scale resolution in real space. Our atomic-resolution imaging provides direct evidence for the diffusion of MA^+ , I^- , and Pb^{2+} under electron beam irradiation, thus providing some insights into understanding ion-migration-induced phase transformations and degradation, and consequently the optimization of device performance. For example, since the gentle irradiation under illumination likely only causes the reversible formation of V_{MA}^- with perovskite structure preserved, accordingly the device efficiency can be fully recovered at early degradation stages⁵⁴. However, longer irradiation brings in I^- and Pb^{2+} diffusion to induce an irreversible transformation into PbI_2 , thus bringing in an irreversible device performance degradation. The irreversible performance decline has also been

observed under elevated temperature^{55,56} and large bias⁵⁷ due to the irreversible ion migration and structure degradation.

In summary, we have acquired the atomic structure of MAPbI₃, determined the threshold doses during TEM characterizations, and clarified the atomic-scale ion migration during its degradation into PbI₂. The degradation pathway is proposed to be a two-step, initiated by the loss of MA⁺ and followed by the diffusion of I⁻ and Pb²⁺ to form PbI₂, during which C–N bonds can be destroyed under irradiation, releasing NH₃ and HI and leaving hydrocarbons. Such degradation process leads to the gradual increase of bandgap. These findings can be used to guide the future TEM characterizations, enrich the understandings of the degradation mechanism and optimization strategies, and provide atomic-scale insights into understanding its fundamental properties.

Methods

MAPbI₃ synthesis. MAPbI₃ nanocrystals were bought from Xiamen Luman Technology Co., Ltd. Micro MAPbI₃ was synthesized as previously reported⁵⁸. Specifically, PbI₂ and MAI were prepared in γ -butyrolactone (GBL) with molar ratio 1:1 and the concentration of 1.3 mol L⁻¹. Then they were stirred at 70 °C for 12 h to obtain the precursor solution. After, the precursor solution was filtered using polytetrafluoroethylene (PTFE) filter with 0.22 μ m pore size. Two pieces of fluorine-doped tin oxide (FTO)/TiO₂ substrates were clamped together and vertically and partially soaked in MAPbI₃ precursor solution (10 ml) at 120 °C. Then the precursor solution was added twice one day in the nitrogen glove box. After several days, the substrates with single-crystal MAPbI₃ film were brought out, and dried at 120 °C for 10 min in nitrogen.

Characterization and image analysis. ED patterns and HRTEM images were acquired at an aberration corrected FEI electron microscope (Titan Cubed Themis G2) operated at 300 kV. The Cs value is \sim 6.8 μ m. Before acquiring images, the illumination range was set to be \sim 3 μ m in diameter. To shorten the exposure time to electron beam, we adjusted the defocus and the astigmatism well in one \sim 3- μ m region, then blanked beam, and moved to another \sim 3- μ m region to acquire the HRTEM image. HRTEM images were acquired at a magnification of 77,000 by DDEC camera in electron-counting mode with the dose fractionation function. The correction of drift was achieved by using the DigitalMicrograph software by cross-correlation. The original image contains 40 subframes in 4 s and every 2 subframes were summed to enhance the contrast for a more accurate estimation of drift. Hanning window and Bandpass filters were combined to improve the accuracy of the cross correlation. HRTEM images in Figs. 1, 2e, and 4, and Supplementary Figs. 2, 6, and 7 have been ABSF-filtered. HRTEM images in Fig. 2a, c have been first ABSF-filtered and then averaged from multiple regions using a home-made MATLAB code to reduce noise.

The morphology was characterized by SEM (FEI Quanta 200 F) and CL spectrum was acquired using Rainbow-CL of Beijing Goldenscope Technology Co., Ltd at 5 kV, spotsize 4. Each single CL spectrum was acquired using 4 s. Vibrational spectra characterizations were obtained under 30 kV using Nion U-HERMES200 electron microscope. Each spectrum was stacked from 200 single spectrum, obtained using 800 ms, and the processing details were shown in Supplementary Fig. 12. The simulated ED patterns were obtained by the SingleCrystal (Crystallmaker) software. Structural models were acquired using Vesta software.

DFT calculation. Our first-principles calculations were performed within the framework of DFT as implemented in the Vienna ab initio simulation package^{59,60}. The ion-electron interaction was depicted by projector augmented-wave method⁶¹. The electron exchange correlation was treated by the generalized gradient approximation with Perdew–Bruke–Ernzerhof functional⁶². A kinetic cutoff energy was set as 500 eV for the Kohn–Sham orbitals being expanded in the plane-wave basis. The atomic positions were fully optimized with a conjugate gradient algorithm until the Hellman–Feynman force on each atom are less than 0.01 eV/Å⁶³. The Monkhorst–Pack k-point meshes was sampled as $9 \times 9 \times 7$ ⁶⁴.

Ab initio molecular dynamics simulation. We performed the ab initio molecular dynamic (AIMD) simulation. The plane-wave cutoff was set as 500 eV and the Brillouin zone is sampled at the Γ point. The AIMD was performed in the canonical ensemble at 300 K.

Data availability

The authors declare that all relevant data are included in the paper and Supplementary Information files and are available from the corresponding author upon reasonable request.

Code availability

Additional data including the codes are available from the corresponding author upon reasonable request.

Received: 22 June 2021; Accepted: 3 September 2021;

Published online: 17 September 2021

References

- Kojima, A., Teshima, K., Shirai, Y. & Miyasaka, T. Organometal halide perovskites as visible-light sensitizers for photovoltaic cells. *J. Am. Chem. Soc.* **131**, 6050–6051 (2009).
- Chen, W. et al. Efficient and stable large-area perovskite solar cells with inorganic charge extraction layers. *Science* **350**, 944 (2015).
- Cao, Y. et al. Perovskite light-emitting diodes based on spontaneously formed submicrometre-scale structures. *Nature* **562**, 249–253 (2018).
- Lin, K. et al. Perovskite light-emitting diodes with external quantum efficiency exceeding 20 per cent. *Nature* **562**, 245–248 (2018).
- Saouma, F. O., Stoumpos, C. C., Wong, J., Kanatzidis, M. G. & Jang, J. I. Selective enhancement of optical nonlinearity in two-dimensional organic-inorganic lead iodide perovskites. *Nat. Commun.* **8**, 742 (2017).
- Fan, Y. et al. Resonance-enhanced three-photon luminescence via lead halide perovskite metasurfaces for optical encoding. *Nat. Commun.* **10**, 2085 (2019).
- Huang, J., Yuan, Y., Shao, Y. & Yan, Y. Understanding the physical properties of hybrid perovskites for photovoltaic applications. *Nat. Rev. Mater.* **2**, 17042 (2017).
- Filip, M. R., Eperon, G. E., Snaith, H. J. & Giustino, F. Steric engineering of metal-halide perovskites with tunable optical band gaps. *Nat. Commun.* **5**, 5757 (2014).
- Milot, R. L., Eperon, G. E., Snaith, H. J., Johnston, M. B. & Herz, L. M. Temperature-dependent charge-carrier dynamics in CH₃NH₃PbI₃ perovskite thin films. *Adv. Funct. Mater.* **25**, 6218–6227 (2015).
- Jiao, Y. et al. Strain engineering of metal halide perovskites on coupling anisotropic behaviors. *Adv. Funct. Mater.* **31**, 2006243 (2021).
- Li, W. et al. Chemically diverse and multifunctional hybrid organic–inorganic perovskites. *Nat. Rev. Mater.* **2**, 16099 (2017).
- Yan, W., Lu, G. & Liu, F. Effect of chlorine substitution on lattice distortion and ferroelectricity of CH₃NH₃PbI₃. *J. Phys. Chem. C* **120**, 17972–17977 (2016).
- National Renewable Energy Laboratory (NREL). Efficiency records chart. <https://www.nrel.gov/pv/cell-efficiency.html>. Accessed Aug 2021.
- Frost, J. M. et al. Atomistic origins of high-performance in hybrid halide perovskite solar cells. *Nano Lett.* **14**, 2584–2590 (2014).
- Huang, B. et al. Polar or nonpolar? That is not the question for perovskite solar cells. *Nat. Sci. Rev.* **8**, nwab094 (2021).
- Zhang, D. et al. Atomic-resolution transmission electron microscopy of electron beam-sensitive crystalline materials. *Science* **359**, 675–679 (2018).
- Song, K. et al. Atomic-resolution imaging of halide perovskites using electron microscopy. *Adv. Energy Mater.* **10**, 1904006 (2020).
- Rothmann, M. U. et al. Structural and chemical changes to CH₃NH₃PbI₃ induced by electron and gallium ion beams. *Adv. Mater.* **30**, 1800629 (2018).
- Chen, S. et al. Atomic scale insights into structure instability and decomposition pathway of methylammonium lead iodide perovskite. *Nat. Commun.* **9**, 4807 (2018).
- Rothmann, M. U. et al. Direct observation of intrinsic twin domains in tetragonal CH₃NH₃PbI₃. *Nat. Commun.* **8**, 14547 (2017).
- Alberti, A. et al. Pb clustering and PbI₂ nanofragmentation during methylammonium lead iodide perovskite degradation. *Nat. Commun.* **10**, 2196 (2019).
- Chen, S. & Gao, P. Challenges, myths, and opportunities of electron microscopy on halide perovskites. *J. Appl. Phys.* **128**, 10901 (2020).
- Deng, Y. Perovskite decomposition and missing crystal planes in HRTEM. *Nature* **594**, E6–E7 (2021).
- Ning, Z. et al. Quantum-dot-in-perovskite solids. *Nature* **523**, 324–328 (2015).
- Rothmann, M. U. et al. Atomic-scale microstructure of metal halide perovskite. *Science* **370**, 548 (2020).
- Zhu, Y. et al. Direct atomic scale characterization of the surface structure and planar defects in the organic-inorganic hybrid CH₃NH₃PbI₃ by Cryo-TEM. *Nano Energy* **73**, 104820 (2020).
- Li, Y. et al. Unravelling degradation mechanisms and atomic structure of organic-inorganic halide perovskites by cryo-EM. *Joule* **3**, 2854–2866 (2019).
- Chen, S. et al. Transmission electron microscopy of organic-inorganic hybrid perovskites: myths and truths. *Sci. Bull.* **65**, 1643–1649 (2020).
- Williams, D. B., Carter, C. B. & Microscopy, C. T. E. *Transmission Electron Microscopy: A Textbook for Materials Science*, 2nd ed. (Springer, New York, 2009).
- Jia, C. L., Lentzen, M. & Urban, K. Atomic-resolution imaging of oxygen in perovskite ceramics. *Science* **299**, 870 (2003).
- Jia, C. L., Houben, L., Thust, A. & Barthel, J. On the benefit of the negative-spherical-aberration imaging technique for quantitative HRTEM. *Ultramicroscopy* **110**, 500–505 (2010).

32. Xiao, C. et al. Mechanisms of electron-beam-induced damage in perovskite thin films revealed by cathodoluminescence spectroscopy. *J. Phys. Chem. C* **119**, 26904–26911 (2015).
33. Rez, P. et al. Damage-free vibrational spectroscopy of biological materials in the electron microscope. *Nat. Commun.* **7**, 10945 (2016).
34. Glaser, T. et al. Infrared spectroscopic study of vibrational modes in methylammonium lead halide perovskites. *J. Phys. Chem. Lett.* **6**, 2913–2918 (2015).
35. Luongo, J. P. Infrared study of polypropylene. *J. Appl. Polym. Sci.* **3**, 302–309 (1960).
36. Gulmine, J. V., Janissek, P. R., Heise, H. M. & Akcelrud, L. Polyethylene characterization by FTIR. *Polym. Test.* **21**, 557–563 (2002).
37. Van Helvoort, K., Knippers, W., Fantoni, R. & Stolte, S. The Raman spectrum of ethane from 600 to 6500 cm^{-1} Stokes shifts. *Chem. Phys.* **111**, 445–465 (1987).
38. Milosavljević, A. R., Huang, W., Sadhu, S. & Ptasińska, S. Low-energy electron-induced transformations in organolead halide perovskite. *Angew. Chem. Int. Ed.* **55**, 10083–10087 (2016).
39. Li, Y. et al. Degradation by exposure of evaporated $\text{CH}_3\text{NH}_3\text{PbI}_3$ thin films. *J. Phys. Chem. C* **119**, 23996–24002 (2015).
40. Röhm, H. et al. Ferroelectric properties of perovskite thin films and their implications for solar energy conversion. *Adv. Mater.* **31**, 1806661 (2019).
41. Gao, P. et al. Picometer-scale atom position analysis in annular bright-field STEM imaging. *Ultramicroscopy* **184**, 177–187 (2018).
42. Song, Z. et al. Probing the origins of photodegradation in organic-inorganic metal halide perovskites with time-resolved mass spectrometry. *Sustain. Energ. Fuels* **2**, 2460–2467 (2018).
43. Merdasa, A. et al. Super-resolution luminescence microspectroscopy reveals the mechanism of photoinduced degradation in $\text{CH}_3\text{NH}_3\text{PbI}_3$ perovskite nanocrystals. *J. Phys. Chem. C* **120**, 10711–10719 (2016).
44. Ouafi, M., Jaber, B., Atourki, L., Bekkari, R. & Laâbnab, L. Improving UV stability of MAPbI_3 perovskite thin films by bromide incorporation. *J. Alloy. Compd.* **746**, 391–398 (2018).
45. Gottesman, R. et al. Photoinduced reversible structural transformations in free-standing $\text{CH}_3\text{NH}_3\text{PbI}_3$ Perovskite Films. *J. Phys. Chem. Lett.* **6**, 2332–2338 (2015).
46. Liu, X. et al. Light-induced degradation and self-healing inside $\text{CH}_3\text{NH}_3\text{PbI}_3$ -based solar cells. *Appl. Phys. Lett.* **116**, 253303 (2020).
47. Hoke, E. T. et al. Reversible photo-induced trap formation in mixed-halide hybrid perovskites for photovoltaics. *Chem. Sci.* **6**, 613–617 (2015).
48. Wang, N. et al. Perovskite light-emitting diodes based on solution-processed self-organized multiple quantum wells. *Nat. Photon* **10**, 699–704 (2016).
49. Zhang, T., Hu, C. & Yang, S. Ion migration: a “double-edged sword” for halide-perovskite-based electronic devices. *Small Methods* **4**, 1900552 (2020).
50. Li, J., Dong, Q., Li, N. & Wang, L. Direct evidence of ion diffusion for the silver-electrode-induced thermal degradation of inverted perovskite solar cells. *Adv. Energy Mater.* **7**, 1602922 (2017).
51. Xia, G. et al. Nanoscale insights into photovoltaic hysteresis in triple-cation mixed-halide perovskite: resolving the role of polarization and ionic migration. *Adv. Mater.* **31**, 1902870 (2019).
52. Divitini, G. et al. In situ observation of heat-induced degradation of perovskite solar cells. *Nat. Energy* **1**, 15012 (2016).
53. Yuan, Y. et al. Electric-field-driven reversible conversion between methylammonium lead triiodide perovskites and lead iodide at elevated temperatures. *Adv. Energy Mater.* **6**, 1501803 (2016).
54. Khenkin, M. V. et al. Dynamics of photoinduced degradation of perovskite photovoltaics: from reversible to irreversible processes. *ACS Appl. Energy Mater.* **1**, 799–806 (2018).
55. Tress, W. et al. Interpretation and evolution of open-circuit voltage, recombination, ideality factor and subgap defect states during reversible light-soaking and irreversible degradation of perovskite solar cells. *Energ. Environ. Sci.* **11**, 151–165 (2018).
56. Mesquita, I., Andrade, L. & Mendes, A. Temperature impact on perovskite solar cells under operation. *ChemSusChem* **12**, 2186–2194 (2019).
57. Bae, S. et al. Electric-field-induced degradation of methylammonium lead iodide perovskite solar cells. *J. Phys. Chem. Lett.* **7**, 3091–3096 (2016).
58. Zhao, J. et al. Single crystalline $\text{CH}_3\text{NH}_3\text{PbI}_3$ self-grown on FTO/ TiO_2 substrate for high efficiency perovskite solar cells. *Sci. Bull.* **62**, 1173–1176 (2017).
59. Kresse, G. & Hafner, J. Ab initio molecular dynamics for open-shell transition metals. *Phys. Rev. B* **48**, 13115 (1993).
60. Furthmüller, J. & Kresse, G. Efficient iterative schemes for ab initio total-energy calculations using a plane-wave basis set. *Phys. Rev. B* **54**, 11169–11186 (1996).
61. Blöchl, P. E. Projector augmented-wave method. *Phys. Rev. B* **50**, 17953 (1994).
62. Perdew, J. P., Burke, K. & Ernzerhof, M. Generalized gradient approximation made simple. *Phys. Rev. Lett.* **77**, 3865–3868 (1996).
63. Grimme, S., Antony, J., Ehrlich, S. & Krieg, H. A consistent and accurate ab initio parametrization of density functional dispersion correction (DFT-D) for the 94 elements H–Pu. *J. Chem. Phys.* **132**, 154104 (2010).
64. Monkhorst, H. J. & Pack, J. D. Special points for Brillouin-zone integrations. *Phys. Rev. B* **13**, 5188 (1976).

Acknowledgements

This work was supported by the National Natural Science Foundation of China (11974023, 52021006, 52125307, 11772207, U2130128, 22003074, 51575135, 51622503, U1537206 and 51621091), the Key R&D Program of Guangdong Province (2018B030327001, 2018B010109009), the “2011 Program” from the Peking-Tsinghua-IOP Collaborative Innovation Center of Quantum Matter, the Guangdong Provincial Key Laboratory Program from the Department of Science and Technology of Guangdong Province (2021B1212040001), Guangdong Basic and Applied Basic Research Foundation (2020A1515110580), the State Key Laboratory of Mechanics and Control of Mechanical Structures (Nanjing University of Aeronautics and Astronautics) (MCMS-E-0420G01), SIAT Innovation Program for Excellent Young Researchers, the Shenzhen Science and Technology Innovation Committee (JCYJ20180507182257563), Natural Science Foundation of Heilongjiang Province of China (YQ2019E023), Natural Science Foundation of Hebei Province for distinguished young scholar (A2019210204) and Central guiding local science and technology development fund projects (216Z4302G). The authors gratefully acknowledge the Electron Microscopy Laboratory at Peking University for the use of electron microscopes and the support of the Center for Computational Science and Engineering at Southern University of Science and Technology. The authors also thank Mr. Yunkun Wang and Prof. Yu-nan Gao at Peking University for Raman test of MAPbI_3 , Prof. Yuan Yao at Institute of Physics, Chinese Academy of Sciences and Dr. Wenquan Ming at Hunan University for helpful discussions about the HRTEM data processing.

Author contributions

P.G., J.L., J.Z. and S.C. conceived the project. P.G. and J.L. supervised the project. S.C. performed TEM experiments, analyzed experimental data and prepared the manuscript with the direction of P.G. and help from J.Q. and J.C. C.W. performed the calculations under the guidance of X.W. B.H. carried out vibrational spectroscopy and Z.L. performed CL measurements. Z.M. and W.H. grew MAPbI_3 crystals under the guidance of J.Z. Q.Z., J.F., K.L. and D.Y. provided additional specimen. S.C., J.L. and P.G. wrote the manuscript and all authors participated in the revision.

Competing interests

The authors declare no competing interests.

Additional information


Supplementary information The online version contains supplementary material available at <https://doi.org/10.1038/s41467-021-25832-9>.

Correspondence and requests for materials should be addressed to Jinjin Zhao, Xiao Wang, Jiangyu Li or Peng Gao.

Peer review information *Nature Communications* thanks Hui-Shu Gavin Tsai and the other, anonymous, reviewer(s) for their contribution to the peer review of this work.

Reprints and permission information is available at <http://www.nature.com/reprints>

Publisher's note Springer Nature remains neutral with regard to jurisdictional claims in published maps and institutional affiliations.

 **Open Access** This article is licensed under a Creative Commons Attribution 4.0 International License, which permits use, sharing, adaptation, distribution and reproduction in any medium or format, as long as you give appropriate credit to the original author(s) and the source, provide a link to the Creative Commons license, and indicate if changes were made. The images or other third party material in this article are included in the article's Creative Commons license, unless indicated otherwise in a credit line to the material. If material is not included in the article's Creative Commons license and your intended use is not permitted by statutory regulation or exceeds the permitted use, you will need to obtain permission directly from the copyright holder. To view a copy of this license, visit <http://creativecommons.org/licenses/by/4.0/>.

© The Author(s) 2021